Quantum phases of strongly interacting bosons on a two-leg Haldane ladder

S. Greschner and F. Heidrich-Meisner

Quantum phases of strongly-interacting bosons on a two-leg Haldane ladder

S. Greschner[1, 2] and F. Heidrich-Meisner[3]

[1]*Institut für Theoretische Physik, Leibniz Universität Hannover, 30167 Hannover, Germany*
[2]*Department of Quantum Matter Physics, University of Geneva, 1211 Geneva, Switzerland*
[3]*Department of Physics and Arnold Sommerfeld Center for Theoretical Physics,*
Ludwig-Maximilians-Universität München, 80333 München, Germany
(Dated: March 2, 2018)

We study the ground-state physics of a single-component Haldane model on a hexagonal two-leg ladder geometry with a particular focus on strongly interacting bosonic particles. We concentrate our analysis on the regime of less than one particle per unit-cell. As a main result, we observe several Meissner-like and vortex-fluid phases both for a superfluid as well as a Mott-insulating background. Furthermore, we show that for strongly interacting bosonic particles an unconventional vortex-lattice phase emerges, which is stable even in the regime of hardcore bosons. We discuss the mechanism for its stabilization for finite interactions by a means of an analytical approximation. We show how the different phases may be discerned by measuring the nearest- and next-nearest-neighbor chiral currents as well as their characteristic momentum distributions.

I. INTRODUCTION

With the rapid progress in the realization of synthetic magnetism in ultracold atomic gases during recent years, experiments in this field are now at the cusp of complementing the theoretical approaches and solid-state experiments on topological effects in *strongly correlated* quantum systems [1, 2]. At the same time, seminal advances in experiments with irradiated graphene [3, 4] or photonic lattices [5–7] have shown the availability of these technologies for the investigation of topological states of matter as well. So far, experiments have succeeded with several proof of concept measurements of various topological effects, most of which, however, studied noninteracting particles. Among these efforts, we mention the quantum engineering of various Hofstadter-Harper like models [8] with staggered [9, 10] or rectified fluxes [11, 12] in ultracold atoms. Highly non-trivial properties can be measured in these experiments such as chiral currents [13–15], Chern numbers [16–18] or Berry curvatures [19–21]. The theoretical understanding of interaction effects of such models, however, remains challenging and has triggered numerous studies in this field. For Hofstadter-Harper like models those include, e.g., predictions of interacting (fractional) Chern insulators [22–27] and other unconventional quantum states [28–32].

Another paradigmatic example of a model with nontrivial topological phases is the famous Haldane model [33], given by the Hamiltonian

$$H_H = -J \sum_{\langle \ell, \ell' \rangle} (c_\ell^\dagger c_{\ell'} + \text{H.c.})$$
$$- J_H \sum_{\langle \langle \ell, \ell' \rangle \rangle} (e^{i\phi_H} c_\ell^\dagger c_{\ell'} + \text{H.c.}), \qquad (1)$$

where c_ℓ ($c_\ell^\dagger$) describes a single-component fermionic or bosonic annihilation (creation) operator, with $\langle \ell, \ell' \rangle$ denoting nearest neighbors and $\langle \langle \ell, \ell' \rangle \rangle$ next-nearest neighbors. A sketch of the model is shown in Fig. 1. Con-

trary to the example of topological states of matter realized in an electronic system with a strong magnetic field [8], here, no net flux pierces the unit-cell of the lattice and, hence, translational symmetry is not explicitly broken. In spite of its apparent complexity - the need of complex next-nearest neighbor exchange terms, which seemed unrealistic from a condensed matter perspective - during recent years, the Haldane (and related) models were realized experimentally using photon-dressed graphene [4], arrays of coupled waveguides [6] and periodically modulated optical lattices [34]. Again, it is of particular interest to understand the interaction effects in this model [35, 36]. For the case of bosonic particles in the Haldane model, He *et al.* [37] have recently shown the emergence of a symmetry-protected bosonic integer quantum Hall phase by means of numerical simulations of large scale cylinders. In Refs. [38, 39], unconventional bosonic chiral superfluid phases have been found.

An important link between theory and the experimental realization of quantum-lattice gases with artificial gauge fields in the strongly correlated regime can
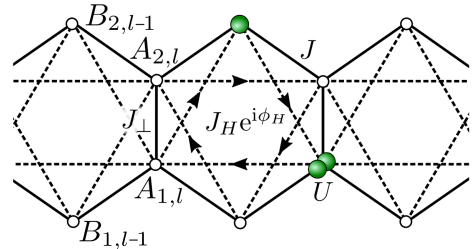

FIG. 1. (Color online) Sketch of the Haldane ladder and the model Eq. (1) for interacting bosonic atoms. Throughout the paper we set $J_\perp = J$. The strength of the next-nearest neighbor tunneling matrix elements is J_H (dashed lines), the phase attached to these links is ϕ_H. The onsite interaction strength is denoted by U. The unit cell contains four sites, denoted by $A_{1,\ell}$, $A_{2,\ell}$, $B_{1,\ell}$, $B_{2,\ell}$, where the first index labels the upper(lower) leg of the ladder.
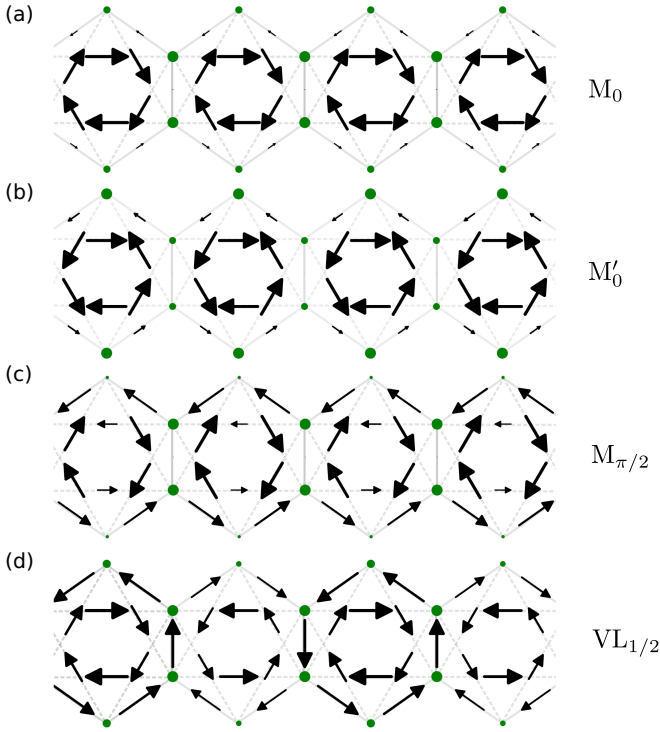
FIG. 2. (Color online) Examples of the different ground-state current configuration in (a)-(c) the three Meissner-like phases found for fermions and bosons and (d) the vortex-lattice phase that exists for strongly interacting bosons. The data are obtained from actual DMRG simulations for the case of hardcore bosons with a filling $\rho = 0.19$, $\phi_H/\pi = 0.95$ and (a) $J_H = 0.12J$ (M_0), (b) $J_H = 0.52J$ (M_0'), (c) $J_H = 1.4J$ ($M_{\pi/2}$), (d) $J_H = 1.12J$ ($VL_{1/2}$). The size of the arrows is proportional to the strength of the currents on the corresponding bond (for clarity, the size of the next-nearest neighbor currents has been reduced by a factor of 2). The size of the circles corresponds to the local onsite density. For the depicted bosonic case, the lengths of the largest arrows correspond to currents with an amplitude of (a) $3 \cdot 10^{-3}J$, (b) $0.01J$, (c) $0.04J$, and (d) $0.16J$.

	j_A	j_B	Δn	c	q	j_R^{avg}	$\mathcal{O}_{\mathrm{DW}}$	$k_{\max}$
M_0	≈ 0	$\lesssim 0$	$\gtrsim 0$	1	1	0	0	0
M_0'	$\lesssim 0$	$\gtrsim 0$	$\lesssim 0$	1	1	0	0	0
$M_{\pi/2}$	$\gtrsim 0$	$\lesssim 0$	$\gtrsim 0$	1	1	0	0	$\pi/2$
V				2	1	0	0	$\pm Q$
$VL_{1/2}$				1	2	>0	>0	$0, \pi/2$

TABLE I. Quantum phases of strongly interacting bosons on the two-leg Haldane ladder studied in this work. The three different Meissner phases M_0, M_0', $M_{\pi/2}$, the vortex-liquid (V) and the vortex lattice $VL_{1/2}$ phases exist either atop superfluid (SF) or Mott-insulating (MI) states - for simplicity here we just list the properties of the SF phases. We also list characteristic properties (see the text for details) such as the central charge c, counting the number of gapless modes, the size q of the effective unit cell in the groundstate (i.e. the number of hexagons), the average local rung current j_R^{avg} (Eq. (10)) and the charge-density order $\mathcal{O}_{\mathrm{DW}}$ (Eq. (11)) in the thermodynamic limit. The statements corresponding to the average currents j_A (Eq. (5)), j_B (Eq. (6)) and the average density difference between A and B sites Δn (Eq. (7)) for the three different Meissner-phases should be understood as a heuristically observed tendency. $k_{\max}$ denotes the position of the largest maximum of the momentum distribution function $n(k)$ (Eq. (12)). For the vortex phase, this typically corresponds to some incommensurate value $0 < Q < \pi/2$.

be established by a reduction of the geometry from a two-dimensional model (which is typically theoretically challenging) to a two-(or multi-)leg ladder system. These quasi-one dimensional models not only allow for an advanced theoretical treatment by means of powerful density matrix renormalization group methods (DMRG) [40, 41] or analytical bosonization techniques [42] but from the experimental perspective, they can be realized using various different implementations. Besides the superlattice method [13] and the use of digital mirror devices [43], various synthetic-lattice dimension approaches [14, 15, 44–47] have been employed. These use a coupling between internal states to realize some or even all lattice directions. While the theoretical interest in ladders with a flux dates back to early studies of Josephson junction arrays [48–51], which was then extended to the strongly interacting regime in a seminal

paper by Orignac and Giamarchi [52], the prospects of experimental realizations with ultracold quantum gases have led to tremendous theoretical activity. In particular, during the past years, the study of the low-dimensional relatives of, for example, the Hofstadter-Harper model on two- or three-leg ladder geometries have attracted a large deal of interest [52–78]. While fermionic systems are equally interesting [53, 54], much work has focussed on the ground-state phase diagram of *bosonic* systems, observing a multitude of phases resulting from the kinetic frustration due to the presence of a homogeneous flux per plaquette. These include three Meissner phases characterized by a uniform edge current as well as commensurate and incommensurate vortex-fluid phases [52, 55, 66]. These phases can be characterized by the behavior of the chiral edge current and bulk currents or are distinct by the spontaneous breaking of a discrete symmetry (see Ref. [75] for an overview). We will refer to the ladders that result from the thin-cylinder limit of the Hofstadter-Harper model as flux ladders. Recent work addresses the possibility of stabilizing low-dimensional relatives of fractional quantum Hall states in ladder systems [62, 63, 77–80].

In this paper we study the ground-state physics of the bosonic Haldane model on a two-leg ladder geometry, which exhibits a rich physics. We will focus our analysis on the low filling regime of less than one particle per unit-cell. We start our analysis with a description of the free-fermion version of the model (1), which allows us to understand some of the ground-state phases, and compare to the properties of hardcore bosons
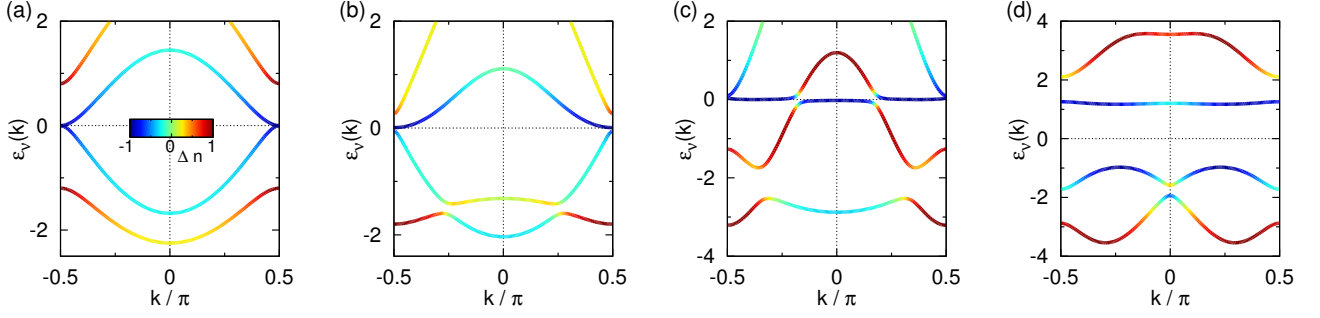
FIG. 3. (Color online) Examples for different single-particle dispersions $\epsilon_\nu(k)$ realized for the two-leg Haldane ladder. In the limit of low fillings, these correspond to the three Meissner phases, (a) M_0 phase ($\phi_H = 0.95\pi$, $J_H = 0.1J$), (b) M_0' phase ($\phi_H = 0.95\pi$, $J_H = 0.4J$), (c) $M_{\pi/2}$ phase ($\phi_H = 0.95\pi$, $J_H = 1.1J$) and (d) the vortex-fluid phase (V) ($\phi_H = 0.6\pi$, $J_H = J$). The color code depicts the density imbalance Δn in the single-particle eigenstates (see Eq. (7)). Note that in the convention of Eq. (3), the first Brillouin zone is defined as $-\pi/2 < k \leq \pi/2$.

$((c_\ell^\dagger)^2 = 0)$. These include Meissner-like states and an incommensurate vortex-fluid phase. The most striking difference compared to free fermions is the emergence of a phase with a broken translational symmetry and the effectively doubled unit-cell in the hardcore boson limit, which we will call vortex-lattice phase $VL_{1/2}$ in analogy to the phases studied for flux ladders [52, 75]. Figure 2 shows representative density and current configurations for the main quantum phases described in this work. By means of DMRG simulations and weak-coupling methods we study the formation of the $VL_{1/2}$ phase for finite on-site interactions $U < \infty$ as well, where the Hamiltonian is augmented by the term

$$H_{\text{int}} = \frac{U}{2} \sum_\ell n_\ell(n_\ell - 1), \qquad (2)$$

with $n_\ell = c_\ell^\dagger c_\ell$. Some exact-diagonalization results for a similar ladder variant of this model have been discussed in [39].

The paper is organized as follows. We start our discussion of the Haldane ladder from the single-particle perspective presented in Sec. II. For the case of free fermions, we introduce the basic properties of the different Meissner-like phases of the model and define relevant observables. In order to give a specific example, we will first fix the phase ϕ_H to be close to π. The case $\phi_H = \pi$ does not exhibit finite local currents (in a finite system), since here time-reversal symmetry is not explicitly broken. We therefore choose $\phi_H = 0.95\pi$ unless stated otherwise. We study the properties and analyze the ground-state phase diagram as a function of the next-nearest-neighbor tunneling amplitude J_H. In the following sections Secs. III-V, we study the behavior of the bosonic model for the same range of parameters starting from the case of hardcore bosons. Here, we focus on the properties of the $VL_{1/2}$ phase, which is one of the main results of this paper. For the case of finite interactions and in Sec. IV, we develop a weak-coupling picture of the emergence of the $VL_{1/2}$ phase, which we compare to numerical simulations. Finally, we discuss the ground-state phase diagram of hardcore bosons as a function of the phase ϕ_H for a fixed amplitude J_H in Sec. V and conclude with a brief summary of our results presented in Sec. VI.

II. SINGLE-PARTICLE SPECTRUM AND FREE FERMIONS

We start our analysis of the model from the free-fermion limit, which allows us to derive an initial picture of some of the liquid phases found also for bosons.

We express the Hamiltonian (1) in momentum space as $H_H = \sum_k \tilde{\boldsymbol{c}}_k^\dagger \mathcal{H}_H(k) \tilde{\boldsymbol{c}}_k$. Here the momentum-space representations of the annihilation operators of the unit cell are grouped into a single vector $\tilde{\boldsymbol{c}}_k$ with $\tilde{\boldsymbol{c}}_k = \sum_\ell e^{2ik} \boldsymbol{c}_\ell$ and $\boldsymbol{c}_\ell^T = \left(c_{A_1,\ell}, c_{A_2,\ell}, c_{B_1,\ell}, c_{B_1,\ell}\right)$ and

$$\mathcal{H}_H(k) = \begin{pmatrix} 2J_H \cos(2k + \phi_H) & J & \left(1 + e^{-2ik}\right) J & 2J_H e^{-ik} \cos(k - \phi_H) \\ J & 2J_H \cos(2k - \phi_H) & 2J_H e^{ik} \cos(k + \phi_H) & \left(1 + e^{-2ik}\right) J \\ \left(1 + e^{2ik}\right) J & 2J_H e^{-ik} \cos(k + \phi_H) & 0 & 0 \\ 2J_H e^{ik} \cos(k - \phi_H) & \left(1 + e^{2ik}\right) J & 0 & 0 \end{pmatrix}. \qquad (3)$$

This can readily be diagonalized leading to $H_H = \sum_{k,\nu=1,...,4} \epsilon_\nu(k) \alpha_{\nu k}^\dagger \alpha_{\nu k}$ with new operators $\alpha_{\nu k} =$

$\sum_{\gamma} \mathcal{U}_{\gamma,k} c_{\gamma,k}$ living on four generally separated energy bands $\epsilon_\nu(k)$ with band index $\nu = 1, 2, 3, 4$.

For $\phi_H \approx \pi$, in particular, we find a rich bandstructure $\epsilon_\nu(k)$. For concreteness and unless stated otherwise, we fix the value of the phase to $\phi_H = 0.95\pi$. Since this is slightly detuned from $\phi_H = \pi$, there are finite chiral currents. We then vary the ratio J_H/J as a free parameter.

Figure 3 shows four examples of the single-particle spectrum for various values of J_H/J and ϕ_H for which different kinds of lowest-band minima are realized: a single minimum at $k = 0$ (Figs. 3 (a) and (b)), a single minimum at $k = \pm\pi/2$ (Fig. 3 (c)) or two degenerate minima at $k = \pm Q$ (Fig. 3 (d)). We may associate these situations to four different low-density ground-state phases - three Meissner-like phases M_0, M_0', $M_{\pi/2}$ and an incommensurate vortex-fluid phase (V), which we will discuss in the following.

We may best characterize the different phases by calculating their local current and density configurations. Due to the explicitly broken time-reversal symmetry of the Hamiltonian (1), quantities of interest are the typically non-vanishing local and average particle currents on nearest-and next-nearest neighbor bonds. A local current $\mathcal{J}(\ell \to \ell')$ from site ℓ to site ℓ' can be derived from the continuity equation $\langle \partial n_\ell / \partial t \rangle = -\sum_{\langle \ell\ell' \rangle} \mathcal{J}(\ell \to \ell') - \sum_{\langle\langle \ell\ell' \rangle\rangle} \mathcal{J}(\ell \to \ell')$.

Examples of the different local current structures in the three Meissner-like states are shown in Figs. 2(a), (b) and (c). Although the data shown are computed for hardcore bosons, the corresponding low-filling free-fermion version of these states looks similar. Since the nearest-neighbor currents $\mathcal{J}(A_{\gamma,\ell} \to B_{\gamma,\ell})$ and $\mathcal{J}(B_{\gamma,\ell} \to A_{\gamma,\ell+1})$ flow in the same direction along the legs, we dub the three phases Meissner phase (M). The inner currents on the rungs $\mathcal{J}(A_{1,\ell} \to A_{2,\ell})$ are strongly suppressed.

In order to make the "Meissner character" of the phases more evident, in Fig. 4, we display the same current configurations for the three different Meissner phases of Fig. 2 with swapped positions of the A sites, i.e., relabeling $A_{1,\ell} \leftrightarrow A_{2,\ell}$. In this notation the strongest current runs through the outer boundary of the ladder system, which is a characteristic signature of a Meissner phase [66].

We may define an average chiral current on the nearest-neighbor bonds as

$$j_c = -\frac{1}{L} \sum_\ell [\mathcal{J}(A_{\gamma,\ell} \to B_{\gamma,\ell}) + \mathcal{J}(B_{\gamma,\ell} \to A_{\gamma,\ell+1})].$$

(4)

In order to take into account the inner currents running on the next-nearest neighbor bonds, we also introduce the average current j_A (j_B) that runs through an A_1 (B_1) site:

$$j_A = -\frac{1}{L} \sum_\ell [\mathcal{J}(A_{1,\ell} \to B_{1,\ell}) + \mathcal{J}(A_{1,\ell} \to A_{1,\ell+1})$$
$$+ \mathcal{J}(A_{1,\ell} \to B_{2,\ell}) + \mathcal{J}(A_{1,\ell} \to A_{2,\ell})]$$
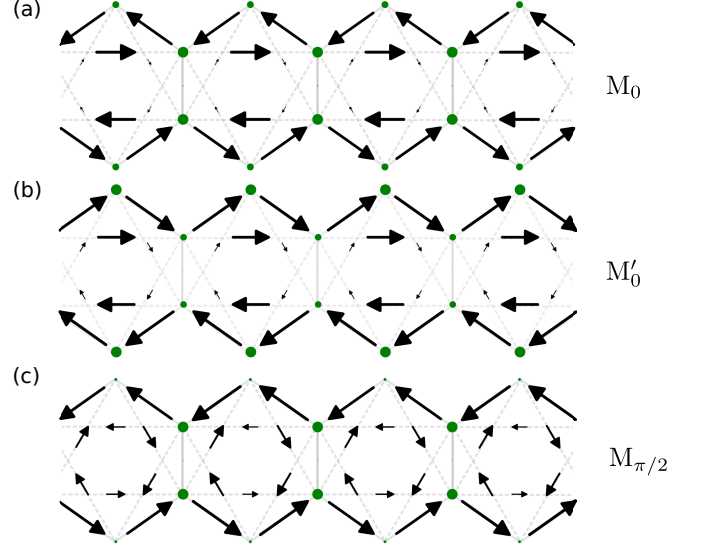
(5)

FIG. 4. (Color online) The same current configurations as in Fig. 2, but the position of A sites has been exchanged, i.e., $A_{1,\ell} \leftrightarrow A_{2,\ell}$. In this way, the Meissner character of the phases (a)-(c) becomes more evident since the strongest currents now flow through the outer boundary of the ladder system.

and

$$j_B = -\frac{1}{L} \sum_\ell [\mathcal{J}(B_{1,\ell} \to A_{1,\ell+1}) + \mathcal{J}(B_{1,\ell} \to A_{2,\ell+1})].$$

(6)

We can understand j_A as an observable that quantifies the average current that runs from one hexagon to the neighboring one, while j_B quantifies the current circulating inside the hexagon.

In the four-site unit cell, the density difference between A and B sites,

$$\Delta n = \frac{1}{L} \sum_{\ell,\gamma=1,2} (n_{A_{\gamma,\ell}} - n_{B_{\gamma,\ell}}),$$

(7)

typically is nonzero. We will refer to Δn as the density imbalance.

In Fig. 5, we show the ground-state phase diagram of free fermions as a function of filling $\rho = N/L$ (up to one particle per unit-cell) and the nearest-neighbor tunneling amplitude J_H/J with extended regions of the M_0, M_0' and $M_{\pi/2}$ phases. In Fig. 6, the current and the density imbalance for a cut through the phase diagram at low filling are depicted. In the M_0 phase, the local currents on the next-nearest-neighbor bonds all circulate in the clockwise direction, opposite to the (small) currents on the nearest-neighbor links. Due to this almost closed ring-current within the hexagon, j_A approximately vanishes in this phase. In the M_0' phase, the sign of the diagonal next-nearest-neighbor currents is flipped compared to the M_0 phase. Hence, also the sign of j_B is inverted
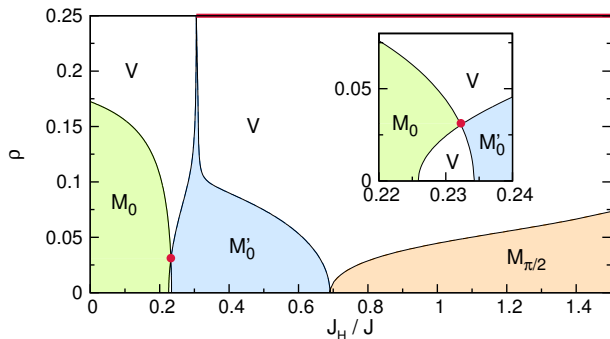
FIG. 5. (Color online) Phase diagram for free spinless fermions in the Haldane ladder ($\phi_H = 0.95\pi$) as a function of density and J_H/J. Three Meissner-like phases exist (M_0, M_0', $M_{\pi/2}$) as well as a vortex fluid phase (V) with incommensurate vortex density. The large red circles mark a Dirac-like point, for which the dispersion relation remains linear.
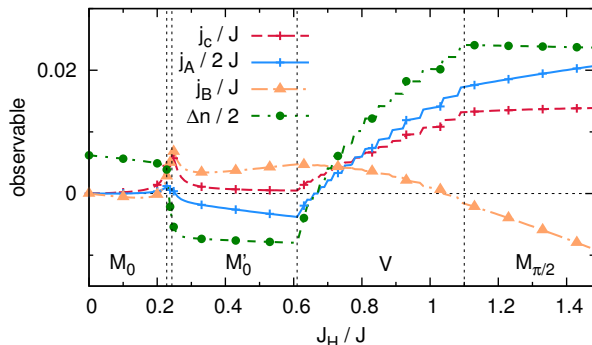

FIG. 6. (Color online) Cut through the phase diagram of free fermions Fig. 5 at a small filling $\rho = 0.05$, showing the currents j_c, $j_A/2$, j_B, and the density imbalance $\Delta n/2$ for a system of $L = 159$ sites. Note that for clarity, less symbols than available data points are shown. Vertical lines indicate the phase boundaries extracted from the bandstructure.

compared to the M_0 phase and we observe a finite inter-hexagon current $j_A < 0$. While in both the M_0 and M_0' phases the chiral current on the outer nearest neighbor bonds j_c is strongly suppressed, the $M_{\pi/2}$ phase is characterized by a larger j_c. Furthermore we find $j_B < 0$ and $j_A > 0$ opposite to the M_0' phase.

The expectation value of Δn may be used to further distinguish the M_0 and M_0' phases from each other (as can be also inferred from the color-code of the dispersion-relations in Fig. 3). The M_0 and $M_{\pi/2}$ phases have $\Delta n > 0$, while $\Delta n < 0$ for the M_0' phase.

For higher fillings (or for special parameters also in the dilute limit) one encounters the situation that more than one Fermi-sea forms, either by occupying modes of an overlapping higher band or because a second local minimum of the same band gets occupied. The doubling of the number of Fermi-points is reflected by a change of the central charge parameter from $c = 1$ to $c = 2$. Due

to the correspondence with the flux-ladder case [52, 66], we generally refer to these phases as vortex fluid phases (V) since the local current structure for a system with open boundary conditions exhibits a strong oscillatory but incommensurate pattern (see Sec. V for a discussion of the analogous vortex-fluid phase for the case of hard-core bosons). Interestingly, for the parameters of Fig. 5 and at the crossing from the M_0 to the M_0' phase, a tiny region with a doubly-degenerate lowest band minimum emerges (see the inset in Fig. 5).

For special parameters, Dirac-like points exist, in which two bands touch with a linear dispersion relation (see the red dot in Fig. 5). While for interacting fermions, nontrivial effects might be expected, for the case of (inter-acting) bosons this feature plays no role since finite-filling properties do not carry over from fermions to bosons. For the filling of one particle per unit cell a trivial band-insulating state is realized for larger values of J_H/J.

III. GROUND-STATE PHASE DIAGRAM FOR HARDCORE BOSONS

In the following we move on to the case of an in-teracting, single-component gas of bosons on the Hal-dane ladder. We start with the case of hardcore bosons ($U/J \to \infty$), which is the simplest case from the numer-ical perspective due to its restricted local Hilbert-space and provides a good starting point to investigate the ef-fect of interactions.

A. Diagnostic tools

Since this model is no longer exactly solvable, we per-form density matrix renormalization group (DMRG) sim-ulations [40, 41, 81] with open boundary conditions to study the ground-state physics of this model keeping up to $\chi = 1000$ DMRG states. We consider various system sizes of odd numbers of rungs L, such that we simulate systems with $(L-1)/2$ hexagons.

Apart from extracting various order parameters, the density imbalance and local currents, our DMRG calcu-lations allow us to study further interesting quantum-information measures. For example, the block entan-glement entropy $S_{vN} = -\text{Tr}[\rho_l \log \rho_l]$, for the reduced density matrix ρ_l of a subsystem of length l may be em-ployed to extract the central charge from the so-called Calabrese-Cardy formula [82–85]

$$S_{vN} = \frac{c}{3} \log \left[\frac{L}{\pi} \sin \frac{\pi l}{L} \right] + \cdots . \tag{8}$$

Phase transitions may also be detected in the finite-size scaling of the fidelity susceptibility [86]

$$\chi_{FS}(J_H) = \lim_{\delta J_H \to 0} \frac{-2 \ln |\langle \Psi_0(J_H)|\Psi_0(J_H + \delta J_H)\rangle|}{(\delta J_H)^2} , \tag{9}$$
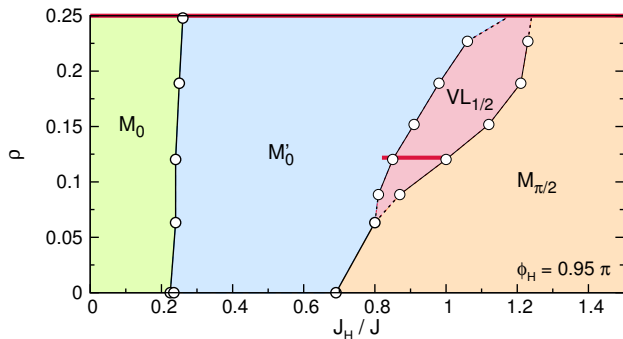
FIG. 7. (Color online) Phase diagram for hardcore bosons in the Haldane ladder for $\phi_H = 0.95\pi$ as a function of density ρ and the next-nearest-neighbor hopping parameter J_H/J. There are three Meissner-like phases (M_0, M_0', $M_{\pi/2}$) as well as a vortex-lattice phase $VL_{1/2}$. At density $\rho = 1/8$, a Mott-insulating state exists in the range $0.75 \lesssim J_H/J \lesssim 1$, while at $\rho = 1/4$, the system is in a Mott-insulating state for any J_H/J.
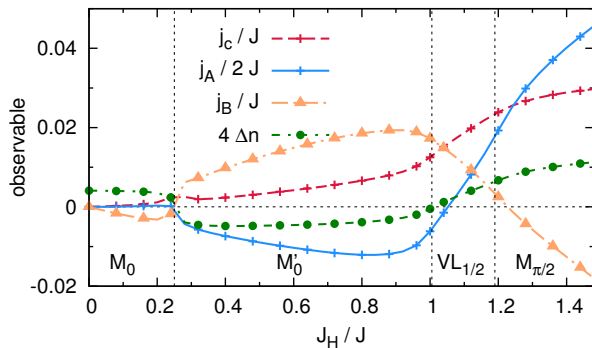

FIG. 8. (Color online) Cut through the phase diagram of hardcore bosons Fig. 7 at density $\rho = 0.19$, showing the currents j_c, $j_A/2$, j_B, and the density imbalance $4\Delta n$.

with $|\Psi_0\rangle$ being the ground-state wave-function.

B. Phase diagram

In Fig. 7 the ground-state phase diagram of hardcore bosons is shown for the parameters of Fig. 5. While in the limit of a dilute lattice gas, the same sequence of ground-state phases as for the case of free fermions is observed, for larger fillings, the differences become more drastic since the incommensurate vortex-fluid phases are suppressed while a vortex-lattice ($VL_{1/2}$) phase gets stabilized, which we will describe in the following Sec. III C in more detail. The current and density structure of this unconventional $VL_{1/2}$ phase is shown in Fig. 2(d).

In Fig. 8, we show several observables and chiral currents for a cut through the phase diagram at a fixed density. As already anticipated in the previous section, the three different Meissner-like phases M_0, M_0' and $M_{\pi/2}$

show a behavior similar to the free-fermion case discussed earlier (see Fig. 6): M_0 and M_0' phases can be discriminated by the sign change of the Δn and j_B observables. While the M_0 phase is characterized by $j_A \approx 0$ and $j_B < 0$, we observe $j_A < 0$ and $j_B > 0$ in the M_0' phase and opposite signs, $j_A > 0$ and $j_B < 0$, in the $M_{\pi/2}$ phase. By means of our numerical simulations we cannot resolve any intermediate phase between the M_0 and M_0' phases at finite densities.

For certain commensurate fillings, namely at $\rho = 1/4$ and for the various Meissner phases but also at $\rho = 1/8$ for the $VL_{1/2}$ phase, a charge gap opens (horizontal thick line in Fig. 7). With this, the sequence of phase transitions becomes very rich, since the M_0, M_0' and $M_{\pi/2}$ phases may be observed on both a superfluid (SF) and a gapped Mott-insulator (MI) background. Contrary to the free-fermion case, we observe the opening of a charge gap at $\rho = 1/4$ for all values of $J_H/J > 0$. At filling $\rho = 1/8$ the MI-phase is apparently confined to the region of the $VL_{1/2}$ phase. From our calculations, we cannot exclude the possibility of a small surrounding region of M_0-MI and $M_{\pi/2}$-MI phases at filling $\rho = 1/8$. Further details of the gapped regions will be discussed below in Sec. V.

C. Vortex-lattice phase

Contrary to the vortex-fluid phases, the $VL_{1/2}$-SF phase is a single-component phase with a central charge $c = 1$ and it exhibits a spontaneously broken translational and parity symmetry. Therefore, the effective unit-cell is doubled as can be seen in Fig. 2(d). An order parameter for the $VL_{1/2}$ phase can be defined from its average local rung-current

$$j_R^{\text{avg}} = \frac{1}{L} \sum_{\ell=0,\ldots,L} |\mathcal{J}(A_{\ell,1} \to A_{\ell,2})| . \tag{10}$$

As an example, we present the finite average rung-current j_R^{avg} in this region in Fig. 9(a). As shown in the insets of Fig. 9(a) the scaling of j_R^{avg} close to the quantum critical points follows Ising-scaling relations and the data points from several finite system-size simulations can be collapsed onto one single curve. As can be seen from the local density pattern shown in Fig. 2(d), the $VL_{1/2}$ phase exhibits a finite density oscillation between adjacent unit-cells. Hence, we may define a charge-density-wave order parameter via

$$\mathcal{O}_{\text{DW}} = \frac{1}{L} \left| \sum_{\ell=0,\ldots,L,\gamma} (-1)^\ell (n_{A_{\ell,\gamma}} + n_{B_{\ell,\gamma}}) \right| . \tag{11}$$

Our numerical calculations indicate that $\mathcal{O}_{\text{DW}}$ stays finite in the thermodynamic limit (see the data for $\mathcal{O}_{\text{DW}}(L)$ shown in Fig. 9(b)), and its L-dependence indeed looks almost identical to the plot of $j_R^{\text{avg}}(L)$ in Fig. 9(a).
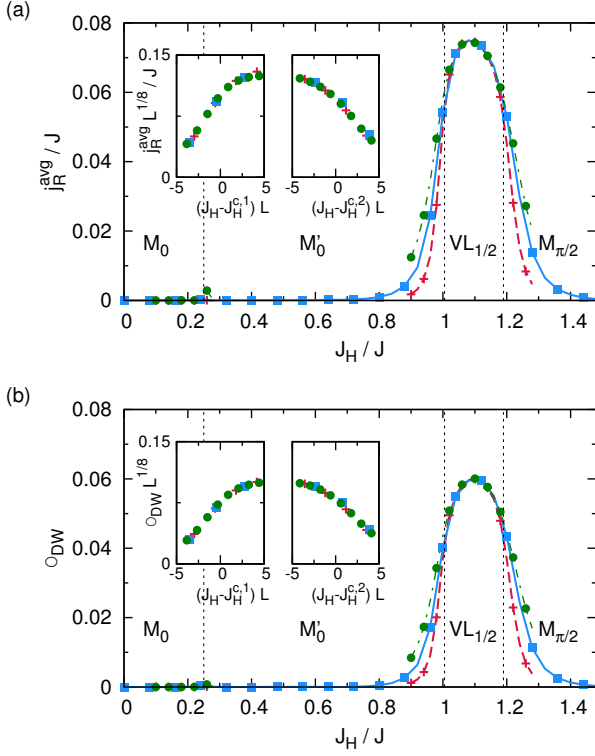
(a)

(b)

FIG. 9. (Color online) Order parameters for the $VL_{1/2}$ phase for a cut through the phase diagram of hardcore bosons Fig. 7 at density $\rho = 0.19$: (a) Average rung-current j_R^{avg} and (b) charge-density order parameter $\mathcal{O}_{\text{DW}}$. The insets depict the collapse of the finite system-size data onto one curve close to the phase-transition points assuming an Ising-type scaling relation. We find $J_H^{c,1} \approx J$ and $J_H^{c,2} \approx 1.19J$ for the left and right boundary of the $VL_{1/2}$ phase, respectively.

A further indication of the Ising character of both the M_0' to $VL_{1/2}$ as well as the $VL_{1/2}$ to $M_{\pi/2}$ transition is the approximate linear divergence of the peak of the fidelity susceptibility $\chi_{FS}/L \propto L$ with system size L as seen in Fig. 10 [87, 88]. Contrary to that, the highly non-linear scaling of the maximum of $\chi_{FS}(J_H)/L$ close to the M_0 to M_0' transition with respect to system size L (see Fig. 9 (a)) may indicate a first-order transition. The same appears to be the case for the M_0'-to-$M_{\pi/2}$ transition at low fillings. However, due to the finite resolution of our calculations, we cannot exclude the possibility of small intermediate phases.

The quasimomentum distribution function

$$n(k) = \frac{1}{L} \sum_{\ell, \ell'} e^{ik(\ell - \ell')} \langle a_\ell^\dagger a_{\ell'} \rangle \qquad (12)$$

is particularly interesting as a possible experimental signature of the $VL_{1/2}$ phase. As shown in Fig. 11, the $VL_{1/2}$-SF phase is characterized by sharp peaks in the quasimomentum distribution at $k = 0$ and $k = \pm\pi/2$.

At incommensurate fillings the $VL_{1/2}$ phase does not exhibit a charge gap and the single-particle correlations
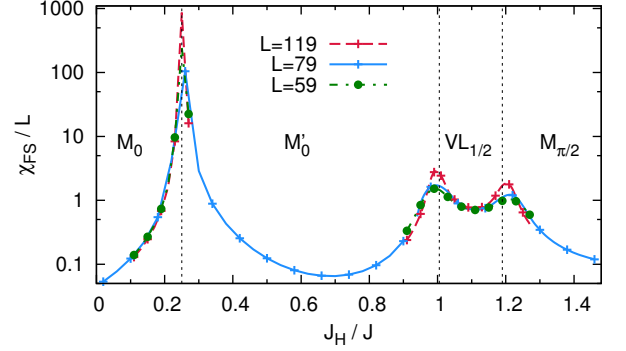

FIG. 10. (Color online) Scaling of the fidelity susceptibility $\chi_{FS}(J_H)/L$ for a cut through the phase diagram of hardcore bosons Fig. 7 at density $\rho = 0.19$. Three phase transitions can be observed at which $\chi_{FS}(J_H)/L$ diverges.
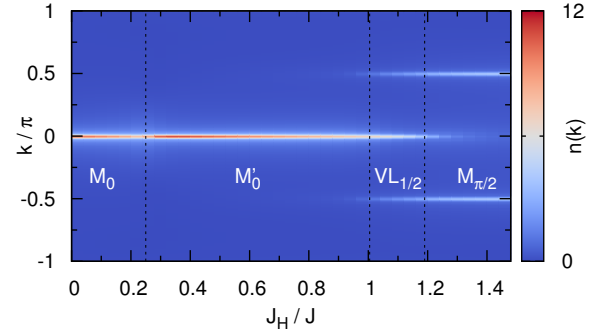

FIG. 11. (Color online) Quasimomentum distribution function $n(k)$ on the legs for the cut through the phase diagram of hardcore bosons Fig. 7 at $\rho = 0.19$. The $VL_{1/2}$ phase is characterized by three distinct peaks at $k = 0$ and $\pm\pi/2$.

decay algebraically (as can also be seen from the presence of sharp peaks in Fig. 11). We may hence understand this liquid $VL_{1/2}$-SF phase with charge-density ordering as another type of a lattice supersolid phase [89–93].

The $VL_{1/2}$ phase may be seen as an analog of the vortex-lattice phase known from the soft-core boson vortex-lattice phases on flux ladders [52, 75], or the so-called chiral phases known from frustrated zig-zag ladders [94]. We want to stress, however, some important differences: The flux-ladder vortex-lattice phases are known to be the most stable for the case of weak interactions and are completely suppressed for the case of hard-core particles on two-leg flux ladders [66]. Here, however, we find the vortex lattice phase even for $U/J \to \infty$.

The zig-zag ladder chiral phases, on the other hand, are best understood from the dilute limit $\rho \to 0$ [95] in which it can be connected to the presence of a two-fold degenerate band-minimum for an extended parameter range, where interactions may favour either a two-component phase or a single-component chiral phase with sponta-
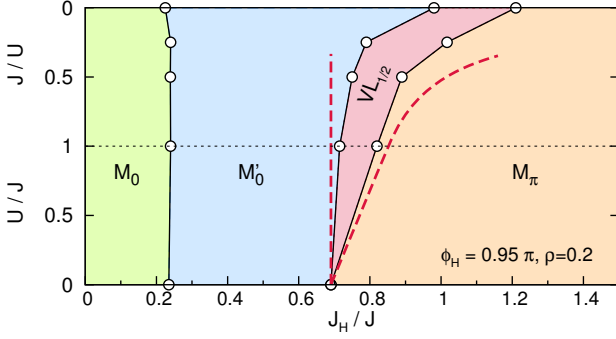
FIG. 12. (Color online) Phase diagram for soft-core bosons in the Haldane ladder as a function of J_H/J and of the interaction strength U/J. Note that for $U > J$, we plot the inverse interaction strength J/U in order to connect the phase boundaries to the hardcore-boson limit. The dashed lines denote the region of instability as predicted from the weak-coupling Bogoliubov approximation (see the text in Sec. IV A).
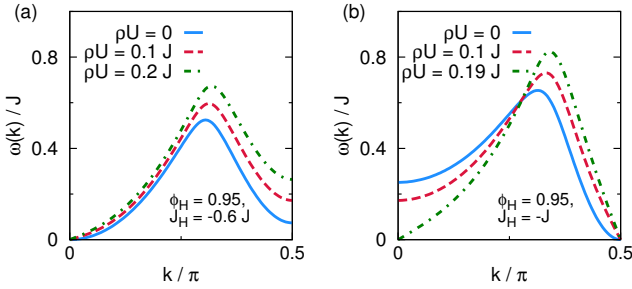

FIG. 13. (Color online) Bogoliubov excitation spectrum $\omega(k)$ for several interaction strengths ρU for $\Phi_H = 0.95\pi$ and (a) $J_H = 0.6J$ and (b) $J_H = J$.

neously broken symmetry between the two dispersion minima. A similar mechanism applies to the so-called biased ladder phase (BLP) on two-leg flux ladder systems [58, 75], which is, however, again most stable for the case of small interactions $U \to 0$.

In the present case of the $VL_{1/2}$ phase on the Haldane ladder, the single-particle spectrum is degenerate only for a single point at $J_H = J_H^c$. As we will motivate in the following section, one may understand this $VL_{1/2}$ phase, naively transferring from the free-fermion case, as a spontaneous breaking of an effective emergent degeneracy between $k = \pi/2$ and $k = 0$ modes due to the finite filling and interactions.

IV. FINITE INTERACTION STRENGTHS $U/J < \infty$

In the following we analyze the stability of the vortex-lattice phase $VL_{1/2}$ for the case of finite repulsive on-site interactions $U/J < \infty$. The main analytical and numerical results are summarized in the phase diagram

of Fig. 12.

A. Limit of weak interactions

In the weak-interaction limit $\rho U \to 0$, we may shed light on the mechanism for the stabilization of the $VL_{1/2}$ phase by means of a simple Bogoliubov-like approximation. We start by projecting the interaction to the lowest band

$$H_{\text{eff}} = \sum_k \epsilon_\alpha(k) \alpha_k^\dagger \alpha_k$$
$$+ \frac{U}{2} \sum_{k,k',q} V_{k+q,k'-q,k,k'} \, \alpha_{k+q}^\dagger \alpha_{k'-q}^\dagger \alpha_k \alpha_k \quad (13)$$

with $V_{k_1,k_2,k_3,k_4} = \sum_{\nu=1\ldots 4} \mathcal{U}_{k_1,\nu}^\dagger \mathcal{U}_{k_2,\nu}^\dagger \mathcal{U}_{k_3,\nu} \mathcal{U}_{k_4,\nu}$, where $\mathcal{U}_{k,\nu}$ is the ν-th eigenvector of the Hamiltonian matrix Eq. (3). As an approximation in the limit of $\rho U \to 0$, we assume a condensation of the bosons at $Q = 0$ (for $J_H \lesssim J_H^c \approx 0.69 \ldots J$) or at $Q = \pi/2$ and with $\alpha_Q \approx \sqrt{N} + \tilde{\alpha}_Q$. Using $\alpha_Q^\dagger \alpha_Q^\dagger \alpha_Q \alpha_Q \approx N^2 - 2N \sum_{k \neq Q} \tilde{\alpha}_k^\dagger \tilde{\alpha}_k$ we rewrite the Hamiltonian retaining only quadratic terms

$$H_{\text{eff}} \approx \sum_k \mathcal{A}(k) \left(\tilde{\alpha}_k^\dagger \tilde{\alpha}_k + \tilde{\alpha}_{-k}^\dagger \tilde{\alpha}_{-k} \right)$$
$$+ \sum_k \mathcal{B}(k) \left(\tilde{\alpha}_k^\dagger \tilde{\alpha}_{-k}^\dagger + \tilde{\alpha}_k \tilde{\alpha}_{-k} \right) \quad (14)$$

with

$$\mathcal{A}(k) = \epsilon(k) - \epsilon(Q) + 4U\rho \left(2V_{Q,k,Q,k} - V_{Q,Q,Q,Q} \right),$$
$$\mathcal{B}(k) = 2U\rho \left(V_{k,-k,Q,Q} + V_{Q,Q,k,-k} \right). \quad (15)$$

A standard Bogoliubov transformation $\beta_k = u_k \tilde{\alpha}_k - v_k \tilde{\alpha}_{-k}^\dagger$ diagonalizes the effective model $H_{\text{eff}} = E_0 + \sum_k \omega(k) \beta_k^\dagger \beta_k$ with $\omega(k) = \sqrt{A(k)^2 - B(k)^2}$, where E_0 is the ground-state energy. Examples of the Bogoliubov-excitation spectra $\omega(k)$ for values of J_H/J in the M_0 and the $M_{\pi/2}$ phases are shown in Fig. 13.

Starting at $U = 0$ from the $M_{\pi/2}$ phase, with increasing interaction ρU, the second minimum of the dispersion relation decreases and at some critical value touches zero at $k = 0$ as is shown in Fig. 13(b). At this point the solution becomes unstable and the approximation of a single condensate at $Q = \pi/2$ is no longer valid. A finite occupation of modes around $k = 0$ has to be taken into account. Hence, we may associate this point of instability with the formation of a phase with a strong interplay between 0 and $\pi/2$ modes, which for large values of ρU can be identified to be the $VL_{1/2}$ phase. Note that the $VL_{1/2}$ phase is characterized by three maxima in the quasimomentum distribution function at $k = 0, \pm\pi/2$. Interestingly, starting from the M_0' phase, the condensate at $Q = 0$ seems to be stabilized with increasing $U\rho$ and the second local minimum at $k = 0$ vanishes upon increasing the interaction strength, as shown in Fig. 13(a).
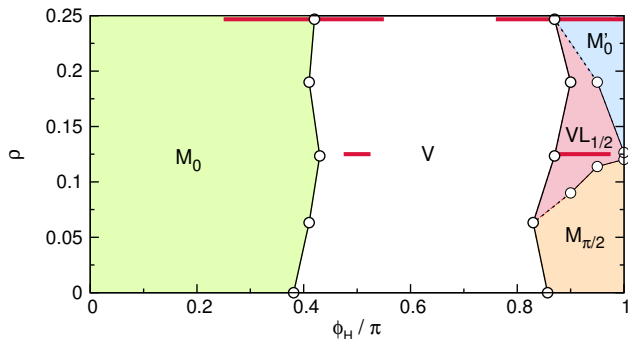
FIG. 14. (Color online) Phase diagram for hardcore-bosons in the Haldane ladder as a function of the phase ϕ_H and the filling ρ for $J_H = J$. At $\rho = 1/4$, there are two regions where the system is in a Mott-insulating state as indicated by the thick horizontal lines.

B.   Comparison to DMRG results

Although the Bogoliubov approach is a crude simplification, we nevertheless obtain a decent qualitative agreement for the phase boundaries of the $VL_{1/2}$ phase with our numerical DMRG results. We employ a cutoff for the occupation of bosons per site of typically $n_{max} = 4$ bosons for $U \gtrsim J$ and fillings $\rho < 1$. By comparison with larger and smaller cutoffs we have ensured the independence of the numerical data on the cutoff for the quantities shown in this work.

The lines of instability of the weak-coupling Bogoliubov method (see Fig. 12) predict a linear opening of the $VL_{1/2}$ phase for $J > J_H^c$, which is consistent with the numerical estimates obtained for a finite filling $\rho = 0.2$ and interaction strength $U \sim J$. Again, for the M_0 to M_0' transition, we do not resolve any intermediate phase in our numerical simulations.

V.   PHASE DIAGRAM AS A FUNCTION OF ϕ_H

In the range of parameters of Fig. 7, we did not find two-component vortex-fluid (V) phases for interacting bosons. However, for different parameters, where a lowest-band minimum exhibits a degeneracy (see Fig. 3 (d)), we observe a bosonic vortex-fluid phase. In Fig. 14, we show the ground-state phase diagram for hardcore bosons as a function of the phase ϕ_H and the density ρ for $J_H = J$. For $0.381 \lesssim \phi_H/\pi \lesssim 0.85$ the minimum is twofold degenerate (compare Fig. 3(d)). Interestingly, almost independently of the filling ρ, a two-component vortex-fluid phase emerges on top of a superfluid background. Exemplary current and density configurations for a cut through the phase diagram Fig. 14 at quarter filling $\rho = 1/4$ are shown in Fig. 15. For large values $\phi_H \sim 0.9\pi$, the $VL_{1/2}$ phase can again be found.

Due to the approximate independence of the boundary of the vortex-fluid phase from the density, it is dif-

ficult to use features of the $\rho(\mu)$ curves (such as shown in Ref. [66]) to extract the position of the phase transition. The boundary of the vortex-fluid phase, however, can also be extracted from a calculation of the central charge [66]. This works best for incommensurate fillings - for the case of commensurate fillings, this becomes more involved as we will discuss in the following.

Experimentally, the vortex-fluid phase may be clearly distinguished from other phases in measurements of the quasimomentum distribution function, in which a multi-peak structure at $\pm Q$ with (in general) $Q \neq 0, \pi/2$ can be observed. We show the corresponding quasimomentum distribution in Fig. 16.

In Fig. 17 we also plot the Fourier transform $F(j_R)$ of the real-space patterns of the rung currents $\langle \mathcal{J}(A_{1,\ell} \to A_{2,\ell}) \rangle(\ell)$. Its distinct peak position may be interpreted as a measure of the vortex-density [66] in the system. As previously shown in Ref. [75] both $F(j_R)$ and the momentum distribution show a similar behavior.

The peak position of $F(j_R)$ in Fig. 17 exhibits a sharp jump for $\phi_H \approx 0.86\pi$, which we here identify as the V to M_0' transition point. Close to this V to M_0' boundary the quasimomentum distribution of Fig. 16 becomes blurred. Interestingly, in this part of the M_0' region, $F(j_R)$ also exhibits a distinct peak at $k > 0$, i.e., finite (boundary driven) oscillations of the rung-currents can still be found. Similar incommensurate Meissner-like-phases have been discussed in Ref. [75] and have been connected to a certain class of Laughlin-precursor states [77, 78] for the case of two-leg flux ladders. Indeed, the presence of such further intermediate phases close to the V to M_0' boundary in this model should be examined in future studies more in detail.

For commensurate fillings, $\rho = 1/8$ and $\rho = 1/4$, we observe the opening of a charge gap for certain values of ϕ_H. This can be the best seen in the $\rho(\mu)$ curves displayed in Fig. 18 for different values of ϕ_H, where small horizontal plateaus at fillings $\rho = 1/4$ and $\rho = 1/8$ indicate the MI-regions.

In Fig. 19 (a) we show the extracted charge gap

$$\Delta_c = \frac{E_0(N-1) - 2E_0(N) + E_0(N+1)}{2}, \qquad (16)$$

extrapolated to the thermodynamic limit $L \to \infty$. Due to the effects of the open boundary conditions the particle density corresponding to the MI-plateau is slightly offset from commensurability, depending on the choice of parameters. We display the data for $N = (L \pm 1)/2$ particles, which corresponds to the largest finite-size value of Δ_c.

Therefore, again, we observe the M_0 and M_0' states and here also the vortex-fluid phases in both the SF and the MI background. For the case of a V - MI phase, we expect the presence of a gapless neutral excitation and, hence, a central charge $c = 1$. In Fig. 19(c) we show the extracted central charge from fits to the entanglement entropy. Examples for the entanglement entropy and its dependence on block size are shown in Fig. 20. The re-
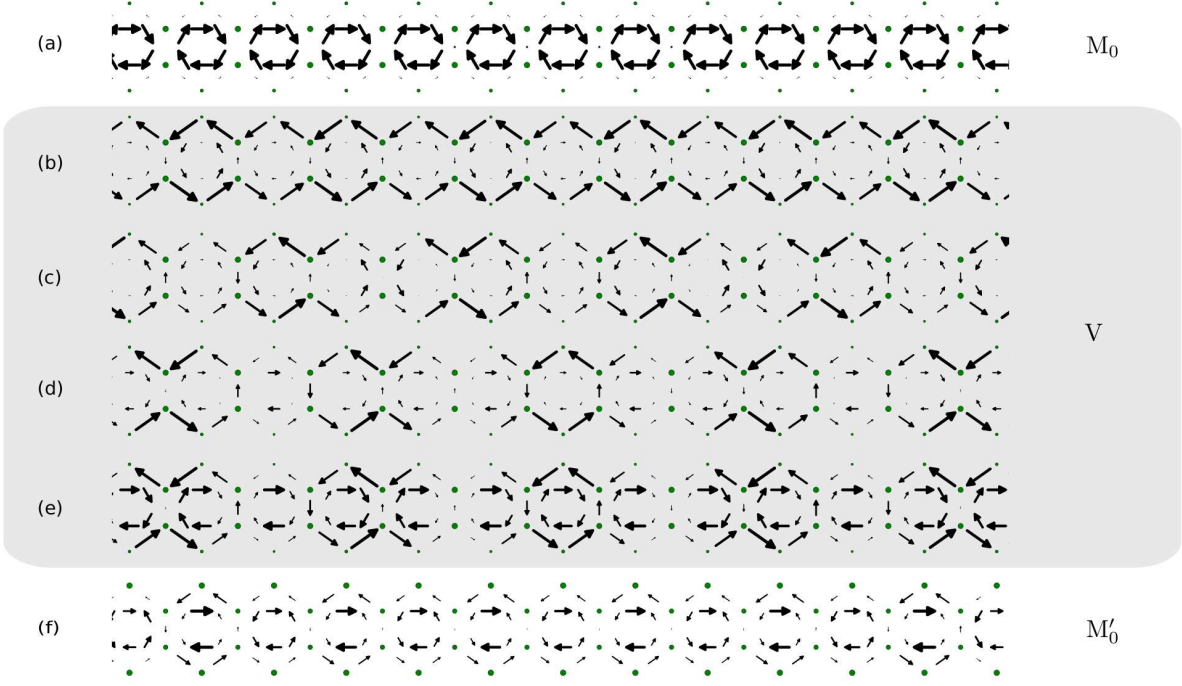
FIG. 15. (Color online) Current and density configurations of the hardcore boson ground state for different values of ϕ_H ($J_H = J$, $\rho = 1/4$). (a) $\phi_H = 0.4\pi$ (M_0 phase), (b-e) $\phi_H = 0.5\pi$, 0.6π, 0.7π, 0.8π (V phase) and (f) $\phi_H = 0.95\pi$ (M_0' phase).
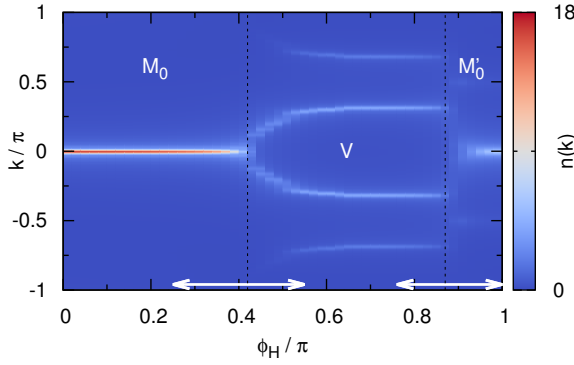

FIG. 16. (Color online) Quasimomentum distribution function $n(k)$ of hardcore bosons as a function of ϕ_H for the parameters of Fig. 14 for $\rho = 0.25$. The arrows denote the estimated extension of the Mott-insulating regions (see Fig. 19).
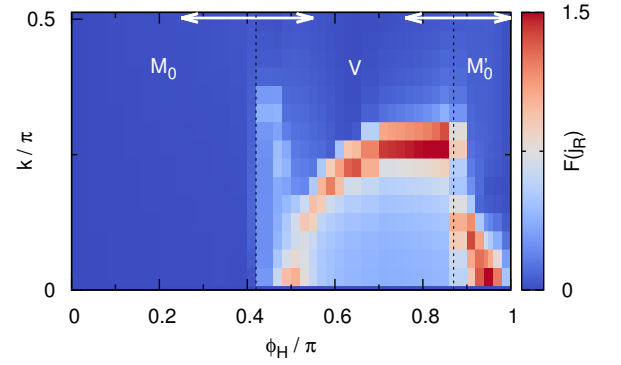
FIG. 17. (Color online) Fourier transform of the real-space pattern of the rung currents $F(j_R)(k)$ as a function of ϕ_H of hardcore bosons for the parameters of Fig. 14 for $\rho = 0.25$.

sults are consistent with $c = 0$ in the M_0- MI and M_0'-MI phases, $c = 1$ in the V- and M_0-SF phases and $c = 2$ in the V-SF phase.

The horizontal arrows in Figs. 16, 17 and 19 show the estimated extension of the MI phases. Due to the Berezinskii-Kosterlitz-Thouless nature of the Mott-insulator to superfluid phase transitions we only give an approximate extension based on the extrapolation of the charge gap and the calculation of the central charge.

In Fig. 19 (c), we plot the behavior of chiral currents and the density imbalance for a cut through the phase diagram Fig. 14 at the commensurate filling $\rho = 1/4$. Consistent with our previous observations, we also find the characteristic features of the Meissner phases: For the M_0 phase, we find j_c and $j_A \approx 0$ and $j_B < 0$ as well as $\Delta n > 0$, while for the M_0' phase we mainly observe opposite signs, $j_B > 0$ and $\Delta n < 0$.
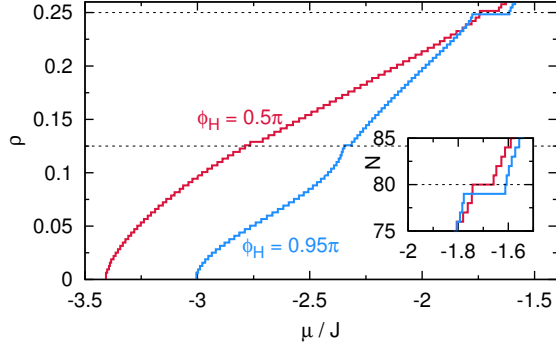
FIG. 18. (Color online) Examples for the equation of state $\rho = \rho(\mu)$ for two cuts through the phase diagram Fig. 14 for $\phi_H = 0.5\pi$ and $\phi_H = 0.95\pi$ ($J_H = J$, $L = 159$ rungs). As discussed in the text, due to the open boundary condition in the finite-system size simulations, the commensurate $\rho = 1/4$ MI plateau is found for $N = 80$ (79) particles for $\phi_H \lesssim 0.9\pi$ ($\phi_H \gtrsim 0.9\pi$). The $\rho(\mu)$ curve for $\phi_H = 0.95\pi$ exhibits a small additional plateau close to filling $\rho = 1/8$. The inset shows a zoom into the region around $\rho = 0.25$ (here, the y-axis shows the total particle number N).

VI. SUMMARY

In summary, we have systematically studied the ground-state phase diagram of interacting bosons (and free fermions) for the Haldane model on a minimal realization of a two-leg ladder. Our main result is the emergence of an exotic type of a vortex-lattice like phase for interacting bosons even for hardcore interactions. The $VL_{1/2}$ phase exhibits a finite rung-current order parameter as well as a finite charge-density wave ordering. Since it emerges both at commensurate fillings with a charge gap but also at a broad range of incommensurate fillings on a superfluid gapless background, in the latter case, the $VL_{1/2}$ phase can be understood as another example of a lattice supersolid, i.e., a liquid with charge-density ordering.

We conclude by pointing future research directions related to this model. In particular, the presence of analogs of Laughlin-precursor states discussed in Refs. [77, 78] may be examined in the region between the vortex-fluid and Meissner phases in the future. Further possible extensions include the analysis of quantum phases in extended lattice geometries such as three-leg ladders and simplified (i.e., no next-to-nearest-neighbor tunneling) brick-wall ladders with a flux that are the thin-torus limit of the hexagonal lattice along the zigzag cut.
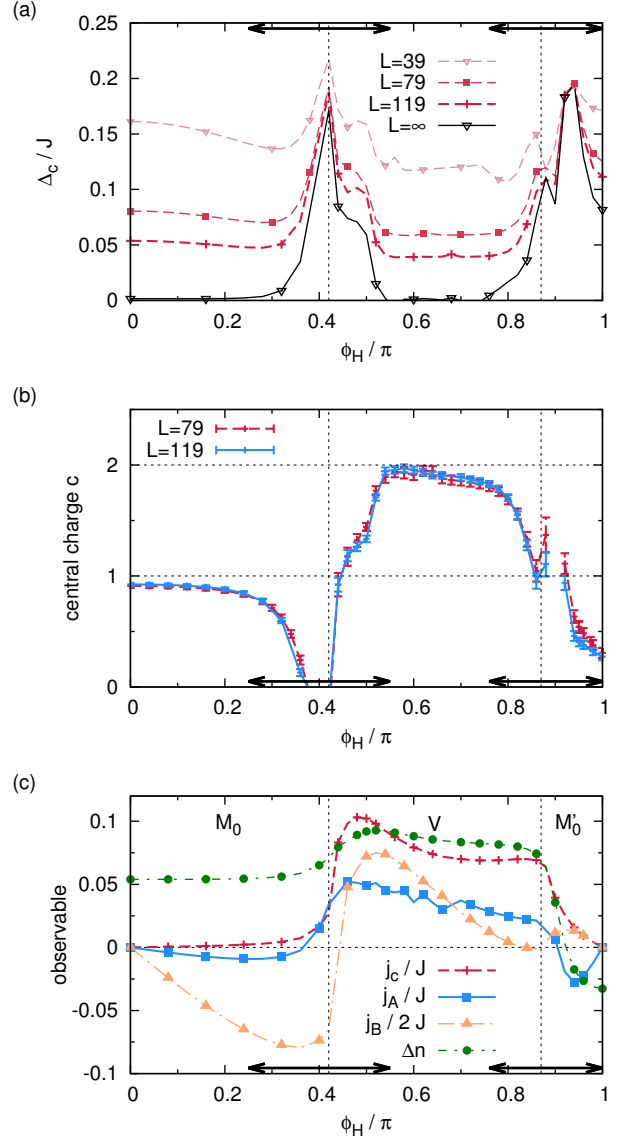
ACKNOWLEDGMENTS

FIG. 19. (Color online) Cut through the phase diagram of hardcore bosons Fig. 14 for $\rho = 0.25$. (a) Charge gap Δ_c for different system sizes as well as an extrapolation to the thermodynamic limit $L \to \infty$ (using a cubic polynomial in $1/L$). (b) Central charge c estimated from a fit to Eq. (8). (c) Average currents j_c, j_A, $j_B/2$, and the density imbalance Δn. The arrows (a)-(c) indicate the extension of the Mott-insulating regions, estimated from a threshold on the extrapolation of the charge gap $\Delta_c/J < 10^{-4}$. The displayed quantities correspond to fillings of $N = (L+1)/2$ particles for $\phi_H < 0.9\pi$ and $N = (L-1)/2$ for $\phi_H > 0.9\pi$ (corresponding to the largest finite-size charge gap).
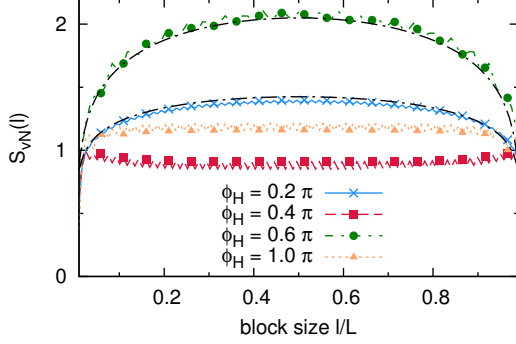
FIG. 20. (Color online) Examples of the entanglement entropy S_{vN} for various values of ϕ_H and hardcore bosons ($J = J_H$, $\rho = 0.25$) corresponding to the $\mathrm{M_0}$-MI ($\phi_H = 0.2\pi$), $\mathrm{M_0'}$-MI ($\phi_H = 0.4\pi$), $\mathrm{M_0}$-SF ($\phi_H = 0.6\pi$) and V-SF ($\phi_H = \pi$) phases. The black dash-dotted lines correspond to a fit to Eq. (8).

[1] V. Galitski and I. Spielman, Nature (London) **494**, 49 (2013).

[2] N. Goldman, J. Budich, and P. Zoller, Nat. Phys. **12**, 639 (2016).

[3] T. Oka and H. Aoki, Phys. Rev. B **79**, 081406 (2009).

[4] Y. Wang, H. Steinberg, P. Jarillo-Herrero, and N. Gedik, Science **342**, 453 (2013).

[5] M. Hafezi, E. A. Demler, M. D. Lukin, and J. M. Taylor, Nat Phys **7**, 907 (2011).

[6] M. C. Rechtsman, J. M. Zeuner, Y. Plotnik, Y. Lumer, D. Podolsky, F. Dreisow, S. Nolte, M. Segev, and A. Szameit, Nature **496**, 196 (2013).

[7] S. Mittal, S. Ganeshan, J. Fan, A. Vaezi, and M. Hafezi, Nat Photon **10**, 180 (2016).

[8] D. R. Hofstadter, Phys. Rev. B **14**, 2239 (1976).

[9] M. Aidelsburger, M. Atala, S. Nascimbène, S. Trotzky, Y.-A. Chen, and I. Bloch, Phys. Rev. Lett. **107**, 255301 (2011).

[10] J. Struck, C. Ölschläger, M. Weinberg, P. Hauke, J. Simonet, A. Eckardt, M. Lewenstein, K. Sengstock, and P. Windpassinger, Phys. Rev. Lett. **108**, 225304 (2012).

[11] H. Miyake, G. A. Siviloglou, C. J. Kennedy, W. C. Burton, and W. Ketterle, Phys. Rev. Lett. **111**, 185302 (2013).

[12] M. Aidelsburger, M. Atala, M. Lohse, J. T. Barreiro, B. Paredes, and I. Bloch, Phys. Rev. Lett. **111**, 185301 (2013).

[13] M. Atala, M. Aidelsburger, M. Lohse, J. T. Barreiro, B. Paredes, and I. Bloch, Nature Phys. **10**, 588 (2014).

[14] B. K. Stuhl, H.-I. Lu, L. M. Aycock, D. Genkina, and I. B. Spielman, Science **349**, 1514 (2015).

[15] M. Mancini, G. Pagano, G. Cappellini, L. Livi, M. Rider, J. Catani, C. Sias, P. Zoller, M. Inguscio, M. Dalmonte, and L. Fallani, Science **349**, 1510 (2015).

[16] M. Aidelsburger, M. Lohse, C. Schweizer, M. Atala, J. T. Barreiro, S. Nascimbne, N. R. Cooper, I. Bloch, and N. Goldman, Nature Phys. **11**, 162166 (2015).

[17] S. Sugawa, F. Salces-Carcoba, A. R. Perry, Y. Yue, and I. B. Spielman, arXiv preprint arXiv:1610.06228 (2016).

[18] M. Lohse, C. Schweizer, H. M. Price, O. Zilberberg, and I. Bloch, Nature **553**, 55 EP (2018).

[19] M. Atala, M. Aidelsburger, J. T. Barreiro, D. Abanin, T. Kitagawa, E. Demler, and I. Bloch, Nature Phys. **9**, 795 (2013).

[20] T. Li, L. Duca, M. Reitter, F. Grusdt, E. Demler, M. Endres, M. Schleier-Smith, I. Bloch, and U. Schneider, Science **352**, 1094 (2016).

[21] N. Fläschner, B. Rem, M. Tarnowski, D. Vogel, D.-S. Lühmann, K. Sengstock, and C. Weitenberg, Science **352**, 1091 (2016).

[22] A. S. Sørensen, E. Demler, and M. D. Lukin, Phys. Rev. Lett. **94**, 086803 (2005).

[23] G. Möller and N. R. Cooper, Phys. Rev. Lett. **103**, 105303 (2009).

[24] N. Regnault and B. A. Bernevig, Phys. Rev. X **1**, 021014 (2011).

[25] T. Neupert, L. Santos, C. Chamon, and C. Mudry, Phys. Rev. Lett. **106**, 236804 (2011).

[26] J. A. Kjäll and J. E. Moore, Phys. Rev. B **85**, 235137 (2012).

[27] G. Möller and N. R. Cooper, Phys. Rev. Lett. **115**, 126401 (2015).

[28] L.-K. Lim, C. M. Smith, and A. Hemmerich, Phys. Rev. Lett. **100**, 130402 (2008).

[29] P. P. Orth, D. Cocks, S. Rachel, M. Buchhold, K. LeHur, and W. Hofstetter, J. Phys. B: At. Mol. Opt. Phys. **46**, 134004 (2012).

[30] J. Radić, A. Di Ciolo, K. Sun, and V. Galitski, Phys. Rev. Lett. **109**, 085303 (2012).

[31] W. S. Cole, S. Zhang, A. Paramekanti, and N. Trivedi, Phys. Rev. Lett. **109**, 085302 (2012).

[32] X. Zhou, Y. Li, Z. Cai, and C. Wu, J. Phys. B:At. Mol. Opt. Phys **46**, 134001 (2013).

[33] F. D. M. Haldane, Phys. Rev. Lett. **61**, 2015 (1988).

[34] G. Jotzu, M. Messer, R. Desbuquois, M. Lebrat, T. Uehlinger, D. Greif, and T. Esslinger, Nature **515**,

237 (2014).

[35] C. N. Varney, K. Sun, M. Rigol, and V. Galitski, Phys. Rev. B **82**, 115125 (2010).

[36] C. N. Varney, K. Sun, M. Rigol, and V. Galitski, Phys. Rev. B **84**, 241105 (2011).

[37] Y.-C. He, S. Bhattacharjee, R. Moessner, and F. Pollmann, Phys. Rev. Lett. **115**, 116803 (2015).

[38] I. Vasić, A. Petrescu, K. Le Hur, and W. Hofstetter, Phys. Rev. B **91**, 094502 (2015).

[39] K. Plekhanov, G. Roux, and K. Le Hur, Phys. Rev. B **95**, 045102 (2017).

[40] S. R. White, Phys. Rev. Lett. **69**, 2863 (1992).

[41] U. Schollwöck, Annals of Physics **326**, 96 (2011).

[42] T. Giamarchi, *Quantum Physics in One Dimension* (Clarendon Press, Oxford, 2004) p. 2905.

[43] M. E. Tai, A. Lukin, M. Rispoli, R. Schittko, T. Menke, D. Borgnia, P. M. Preiss, F. Grusdt, A. M. Kaufman, and M. Greiner, Nature **546**, 519 (2017).

[44] A. Celi, P. Massignan, J. Ruseckas, N. Goldman, I. Spielman, G. Juzeliunas, and M. Lewenstein, Phys. Rev. Lett. **112**, 043001 (2014).

[45] L. F. Livi, G. Cappellini, M. Diem, L. Franchi, C. Clivati, M. Frittelli, F. Levi, D. Calonico, J. Catani, M. Inguscio, and L. Fallani, Phys. Rev. Lett. **117**, 220401 (2016).

[46] S. Kolkowitz, S. L. Bromley, T. Bothwell, M. L. Wall, G. E. Marti, A. P. Koller, X. Zhang, A. M. Rey, and J. Ye, Nature **542**, 66 (2017).

[47] F. A. An, E. J. Meier, and B. Gadway, Science Advances **3** (2017), 10.1126/sciadv.1602685.

[48] M. Kardar, Phys. Rev. B **33**, 3125 (1986).

[49] E. Granato, Phys. Rev. B **42**, 4797 (1990).

[50] J. J. Mazo, F. Falo, and L. M. Floria, Phys. Rev. B **52**, 10433 (1995).

[51] C. Denniston and C. Tang, Phys. Rev. Lett. **75**, 3930 (1995).

[52] E. Orignac and T. Giamarchi, Phys. Rev. B **64**, 144515 (2001).

[53] S. T. Carr, B. N. Narozhny, and A. A. Nersesyan, Phys. Rev. B **73**, 195114 (2006).

[54] G. Roux, E. Orignac, S. R. White, and D. Poilblanc, Phys. Rev. B **76**, 195105 (2007).

[55] A. Petrescu and K. Le Hur, Phys. Rev. Lett. **111**, 150601 (2013).

[56] A. Tokuno and A. Georges, New J. Phys. **16**, 073005 (2014).

[57] D. Hügel and B. Paredes, Phys. Rev. A **89**, 023619 (2014).

[58] R. Wei and E. J. Mueller, Phys. Rev. A **89**, 063617 (2014).

[59] S. Uchino and A. Tokuno, Phys. Rev. A **92**, 013625 (2015).

[60] S. Barbarino, L. Taddia, D. Rossini, L. Mazza, and R. Fazio, Nature Comm. **6**, 8134 (2015).

[61] T.-S. Zeng, C. Wang, and H. Zhai, Phys. Rev. Lett. **115**, 095302 (2015).

[62] A. Petrescu and K. Le Hur, Phys. Rev. B **91**, 054520 (2015).

[63] E. Cornfeld and E. Sela, Phys. Rev. B **92**, 115446 (2015).

[64] S. K. Ghosh, U. K. Yadav, and V. B. Shenoy, Phys. Rev. A **92**, 051602 (2015).

[65] Z. Yan, S. Wan, and Z. Wang, Scientific Reports **5**, 15927 (2015).

[66] M. Piraud, F. Heidrich-Meisner, I. P. McCulloch, S. Greschner, T. Vekua, and U. Schollwöck, Phys. Rev. B **91**, 140406(R) (2015).

[67] M. Di Dio, S. De Palo, E. Orignac, R. Citro, and M.-L. Chiofalo, Phys. Rev. B **92**, 060506 (2015).

[68] F. Kolley, M. Piraud, I. McCulloch, U. Schollwöck, and F. Heidrich-Meisner, New J. Phys. **17**, 092001 (2015).

[69] S. Natu, Phys. Rev. A **92**, 053623 (2015).

[70] A. Keleş and M. O. Oktel, Phys. Rev. A **91**, 013629 (2015).

[71] L. Taddia, E. Cornfeld, D. Rossini, L. Mazza, E. Sela, and R. Fazio, Phys. Rev. Lett. **118**, 230402 (2017).

[72] S. Uchino, Phys. Rev. A **93**, 053629 (2016).

[73] S. K. Ghosh, S. Greschner, U. K. Yadav, T. Mishra, M. Rizzi, and V. B. Shenoy, Phys. Rev. A **95**, 063612 (2017).

[74] E. Anisimovas, M. Račiūnas, C. Sträter, A. Eckardt, I. B. Spielman, and G. Juzeliūnas, Phys. Rev. A **94**, 063632 (2016).

[75] S. Greschner, M. Piraud, F. Heidrich-Meisner, I. P. McCulloch, U. Schollwöck, and T. Vekua, Phys. Rev. A **94**, 063628 (2016).

[76] E. Orignac, R. Citro, M. Di Dio, and S. De Palo, Phys. Rev. B **96**, 014518 (2017).

[77] A. Petrescu, M. Piraud, G. Roux, I. P. McCulloch, and K. Le Hur, Phys. Rev. B **96**, 014524 (2017).

[78] M. Calvanese Strinati, E. Cornfeld, D. Rossini, S. Barbarino, M. Dalmonte, R. Fazio, E. Sela, and L. Mazza, Phys. Rev. X **7**, 021033 (2017).

[79] F. Grusdt and M. Höning, Phys. Rev. A **90**, 053623 (2014).

[80] S. Greschner and T. Vekua, Phys. Rev. Lett. **119**, 073401 (2017).

[81] U. Schollwöck, Rev. Mod. Phys. **77**, 259 (2005).

[82] C. Holzhey, F. Larsen, and F. Wilczek, Nuclear Physics B **424**, 443 (1994).

[83] G. Vidal, J. I. Latorre, E. Rico, and A. Kitaev, Phys. Rev. Lett. **90**, 227902 (2003).

[84] V. Korepin, Phys. Rev. Lett. **92**, 096402 (2004).

[85] P. Calabrese and J. J. Cardy, J. Stat. Mech.: Theory Exp. , P06002 (2004).

[86] S.-J. Gu, Int. J. Mod. Phys. B **24**, 4371 (2010).

[87] L. Campos Venuti and P. Zanardi, Phys. Rev. Lett. **99**, 095701 (2007).

[88] S. Greschner, A. Kolezhuk, and T. Vekua, Phys. Rev. B **88**, 195101 (2013).

[89] A. Andreev and I. Lifshits, Sov. Phys. JETP. **29**, 1107 (1969).

[90] N. Prokofev and B. Svistunov, Phys. Rev. Lett. **94**, 155302 (2005).

[91] G. Batrouni, F. Hébert, and R. Scalettar, Phys. Rev. Lett. **97**, 087209 (2006).

[92] L. Pollet, J. Picon, H. Büchler, and M. Troyer, Phys. Rev. Lett. **104**, 125302 (2010).

[93] R. Landig, L. Hruby, N. Dogra, M. Landini, R. Mottl, T. Donner, and T. Esslinger, Nature **532**, 476 (2016).

[94] S. Greschner, L. Santos, and T. Vekua, Phys. Rev. A **87**, 033609 (2013).

[95] A. K. Kolezhuk, F. Heidrich-Meisner, S. Greschner, and T. Vekua, Phys. Rev. B **85**, 064420 (2012).